ChemComm

COMMUNICATION

View Article Online
View Journal | View Issue

Cite this: *Chem. Commun.*, 2025, **61**, 121

Received 15th October 2024,
Accepted 25th November 2024

DOI: 10.1039/d4cc05467a

rsc.li/chemcomm

An innovative BiOI@$AgBiS_2$@$NaYF_4$:Yb, Tm ternary heterostructure for efficient solar energy harvesting towards tetracycline hydrochloride degradation†

Jinyuan Zhang,[a] Qincan Ma,[a] Junhao Ma,[a] Shuang Fu,[a] Ziyang Ren,[a] Xianzhong Lin *[a] and Yueli Zhang *[ab]

This study developed a BiOI@$AgBiS_2$@$NaYF_4$:Yb,Tm heterostructure photocatalyst. This design significantly enhances the generation and separation of charge carriers, leading to a marked improvement in solar energy harvesting. This advancement was effectively applied for the degradation of tetracycline hydrochloride. This strategy provides inspiration for designing and developing full-spectrum responsive photocatalysts.

Photocatalytic technology, notable for its eco-friendly attributes, utilizes solar energy to degrade pollutants in wastewater into harmless molecules, playing a crucial role in advancing environmental and energy sustainability.[1,2] The semiconductor photocatalyst is the core of photocatalytic technology.

BiOI exhibits a distinctive layered crystal structure, which includes two halogen atomic layers interspersed with various bismuth oxide layers ($[Bi_2O_2]^{2+}$, $[Bi_3O_4]$ or $[Bi_{12}O_{17}]^{2+}$).[3] This structure facilitates the creation of an internal electric field, effectively enhancing the separation of electron–hole pairs.[4] Due to its ultra-thin structure, high specific surface area, and narrow band gap, BiOI exhibits significant potential in photocatalytic pollutant decomposition and CO_2 reduction.[5,6] Nonetheless, its efficacy is limited by a high electron–hole recombination rate. It is crucial to enhance the photocatalytic performance of BiOI photocatalytic performance by employing strategies that effectively mitigate this recombination issue. A crucial strategy in semiconductor heterojunction construction involves altering the charge carriers' migration path.[7,8] This adjustment enhances carrier retention at highly active redox positions, substantially increasing migration velocity and inhibiting recombination. Consequently, this approach markedly enhances photocatalytic efficiency.

$AgBiS_2$, a ternary semiconductor with a narrow band gap, high absorption coefficient (10^5 cm^{-1}),[9] and good stability, exhibits potential in photoelectric detection,[10] solar cell[11] and pollutant decomposition[12] applications. The integration of $AgBiS_2$ onto BiOI, forming BiOI@$AgBiS_2$ heterojunctions, may significantly boost light absorption and reduce carrier recombination, thereby enhancing photoelectric performance.

Semiconductor photocatalysts' poor absorption of near-infrared (NIR) light hinders the efficient utilization of sunlight, which constitute up to 50% of solar energy.[13] This limitation can be addressed by employing upconversion materials that exploit anti-Stokes optical properties to transform low-energy photons into high-energy ones.[14] Specifically, Yb^{3+} sensitized ions within these particles absorb NIR light around 980 nm, facilitating ultraviolet (UV) and visible light emission through energy transfer to Er^{3+} or Tm^{3+} activated ions.[15,16] The enhanced light absorption of composite photocatalysts utilizing upconversion materials and semiconductors is typically ascribed to the upconversion components of previous reports.[17–19] However, studies on improving photocatalytic performance by expanding the light absorption range through dual approaches remain scarce. Consequently, integrating multiple materials into a unified system offers a promising approach to enhance functionality and overcome the constraints associated with single-material systems.

In this study, BiOI, $AgBiS_2$, and $NaYF_4$:Yb,Tm were synthesized using the hydrothermal method. A synthesis strategy for BiOI@$AgBiS_2$ (BABS) heterojunctions was developed. Subsequently, BABS were loaded onto $NaYF_4$:Yb,Tm to create a BiOI@$AgBiS_2$@$NaYF_4$:Yb,Tm (BABS-Tm) ternary composite photocatalyst through mechanical grinding and ultrasonic treatment. The photocatalytic performance of BABS and BABS-Tm was evaluated by degrading tetracycline (TC).

The X-ray diffraction (XRD) patterns of BiOI, $AgBiS_2$, and $NaYF_4$:Yb,Tm match the standard cards of BiOI (PDF #10-0445), $AgBiS_2$ (#89-2045), and β-$NaYF_4$ (#16-0334) without detectable

[a] *State Key Laboratory of Optoelectronic Materials and Technologies, School of Materials Science and Engineering, Sun Yat-sen University, Guangzhou 510275, P. R. China. E-mail: linxzh8@mail.sysu.edu.cn*
[b] *School of Integrated Circuit, Sun Yat-sen University, ShenZhen 518107, P. R. China. E-mail: stszyl@mail.sysu.edu.cn*

† Electronic supplementary information (ESI) available. See DOI: https://doi.org/10.1039/d4cc05467a

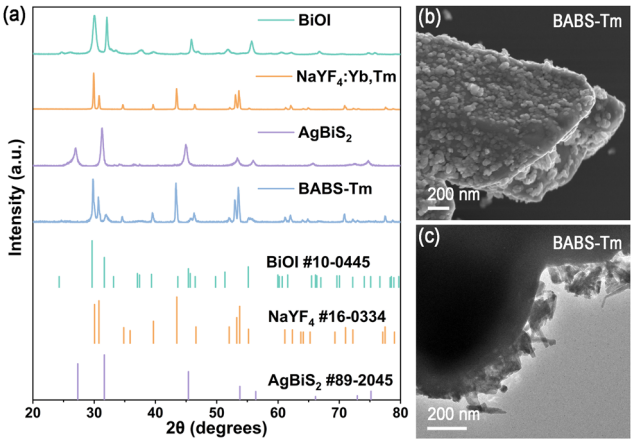

Fig. 1 (a) XRD patterns of BiOI, $AgBiS_2$, $NaYF_4$:Yb,Tm and BABS-Tm. (b) SEM image of BABS-Tm. (c) TEM image of BABS-Tm.

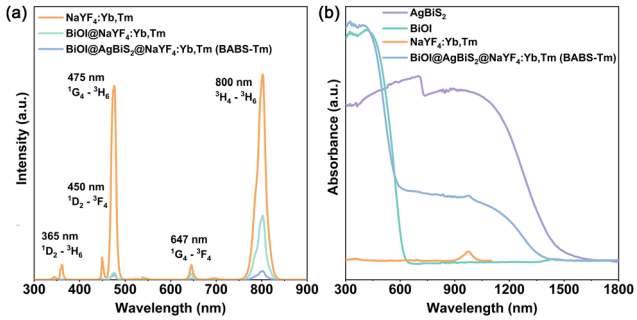

Fig. 2 (a) PL spectra of $NaYF_4$:Yb,Tm, BiOI@$NaYF_4$:Yb,Tm and BABS-Tm under 980 nm irradiation. (b) DRS spectra of BiOI, $AgBiS_2$, $NaYF_4$:Yb,Tm and BABS-Tm.

impurities (Fig. 1(a)), confirming the successful synthesis of pure BiOI, $AgBiS_2$, and $NaYF_4$:Yb,Tm. In the BABS-(2–15%) samples (Fig. S1, ESI†), the primary diffraction peak corresponds to BiOI, with the $AgBiS_2$ (111) plane appearing at 27.3° as the $AgBiS_2$ content increases. Notably, BABS-Tm ternary composite heterostructures exhibit only BiOI and $NaYF_4$:Yb,Tm phases, attributed to a low proportion of $AgBiS_2$.

Scanning electron microscopy (SEM) and transmission electron microscopy (TEM) were utilized to examine the composite samples' morphology. Fig. S2 (ESI†) illustrates that BABS consists of 20–50 nm nanosheets. BABS's energy dispersive spectroscopy (EDS) analysis confirmed the uniform distribution of Bi, S, Ag, and I elements, indicating adequate bonding between BiOI and $AgBiS_2$. Pure $NaYF_4$:Yb,Tm features microrods with a smooth surface morphology, as depicted in Fig. S3 (ESI†). Incorporating BABS onto $NaYF_4$:Yb,Tm results in its surface being entirely covered, as shown in Fig. 1(b) and (c). This coverage forms a tight contact structure on the surface of $NaYF_4$:Yb,Tm, facilitating efficient upconversion energy transfer.

TEM analysis reveals that both BiOI and $AgBiS_2$ possess a nanosheet morphology (Fig. S4 (a)–(c), ESI†). Additionally, high-resolution TEM images of BABS-Tm (Fig. S4(e), ESI†) demonstrate lattice spacings of 0.515 nm, 0.297 nm, 0.205 nm and 0.325 nm, corresponding to the (100) and (110) planes of $NaYF_4$:Yb,Tm, the (113) plane of BiOI, and the (111) plane of $AgBiS_2$, respectively, indicating the successful synthesis of BABS-Tm.

X-ray photoelectron spectroscopy (XPS) was utilized to investigate the valence states of elements and their binding states in materials. The detection of Bi, O, I, Ag, Bi, and S elements in the samples confirms the successful synthesis of BiOI and $AgBiS_2$ (Fig. S5(a) and (b), ESI†). Notably, although Ag and S signals were less pronounced in the BABS sample (Fig. S5(c), ESI†), they were still identifiable in the high-resolution XPS spectra. Comparative analysis of the high-resolution XPS spectra of Bi in BiOI, $AgBiS_2$ and BABS (Fig. S5(d), ESI†) revealed peaks at 164.1 eV and 158.8 eV, corresponding to the Bi $4f_{5/2}$ and Bi $4f_{7/2}$ orbitals of Bi^{3+}, respectively.[20] A notable peak of S 2p is observed in the high-resolution Bi spectrum of $AgBiS_2$. Analysis from Fig. S5(e) (ESI†) assigns the 630.8 eV and 619.4 eV peaks to the I $3d_{3/2}$ and I $3d_{5/2}$ orbitals of I^-, respectively.[21] Constructing a BABS heterojunction results in a 0.5 eV reduction in I's binding energy. Concurrently, the binding energies of Ag $3d_{3/2}$ and Ag $3d_{5/2}$, located at 373.2 eV and 367.2 eV, increase by 0.6 eV post-heterojunction formation (Fig. S5(f), ESI†). The decrease of I^- binding energy and the increase of Ag^- binding energy indicates the strong interaction between BiOI and $AgBiS_2$, indicating the successful formation of a heterojunction.

Fig. 2(a) illustrates the photoluminescence (PL) spectra comparisons among $NaYF_4$:Yb,Tm, BiOI@$NaYF_4$:Yb,Tm, and BABS-Tm. It highlights that the observed luminescence at 365 nm, 450 nm, 475 nm, 647 nm and 800 nm corresponds to the transitions of $^1D_2$–$^3H_6$, $^1D_2$–$^3F_4$, $^1G_4$–$^3H_6$, $^1G_4$–$^3F_4$, and $^3H_4$–$^3H_6$ of the Tm^{3+} energy levels, respectively.[22,23] BiOI and BABS exhibit similar light absorption capabilities towards $NaYF_4$:Yb,Tm in the visible light spectrum. However, the reduced luminescence intensity of BABS-Tm at 647 nm and 800 nm, compared to BiOI@$NaYF_4$:Yb,Tm, suggests that the BABS heterojunction possesses superior light absorption properties than BiOI. Fig. 2(b) illustrates the samples' absorption spectra, revealing distinct band-edge absorptions of BiOI and $AgBiS_2$ which are located at 650 nm and 1500 nm, respectively. $NaYF_4$:Yb,Tm shows the absorption capacity of 980 nm light, corresponding to the transitions of the $^2F_{7/2}$–$^2F_{5/2}$ of Yb^{3+} energy level.[24] Notably, the spectrum of BABS-Tm combines the absorption features of BiOI, $AgBiS_2$, and $NaYF_4$:Yb,Tm, evidencing the effective recombination of BABS-Tm.

This study assessed the photocatalytic degradation of TC by BABS and BABS-Tm. As shown in Fig. S6(a) (ESI†), when the proportion of $AgBiS_2$ is 2%, BABS exhibits the best photocatalytic ability. Despite superior light absorption of $AgBiS_2$, its high electron–hole recombination rate negates the benefits of higher $AgBiS_2$ proportions. Consequently, the BABS-2% formulation was chosen for combination with $NaYF_4$:Yb,Tm. The influences of TC concentration and the dosages of the BABS catalyst on photocatalytic efficiency are analyzed in Fig. S6(b) and (c) (ESI†). The study revealed that increasing the BABS dosage from 2.5 to 7.5 mg significantly enhanced the TC removal rate from 37% to 75%. Beyond a 7.5 mg dosage, the increment in TC

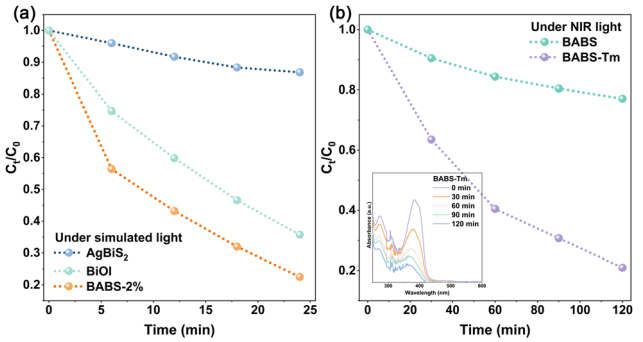

Fig. 3 (a) Photodegradation efficiency of BiOI, $AgBiS_2$ and BABS under simulated solar light irradiation (UV-vis-NIR). (b) Photodegradation efficiency of BABS and BABS-Tm under NIR light irradiation (>780 nm). (Inset: UV-vis adsorption spectra of TC solution as a function of time upon NIR light).

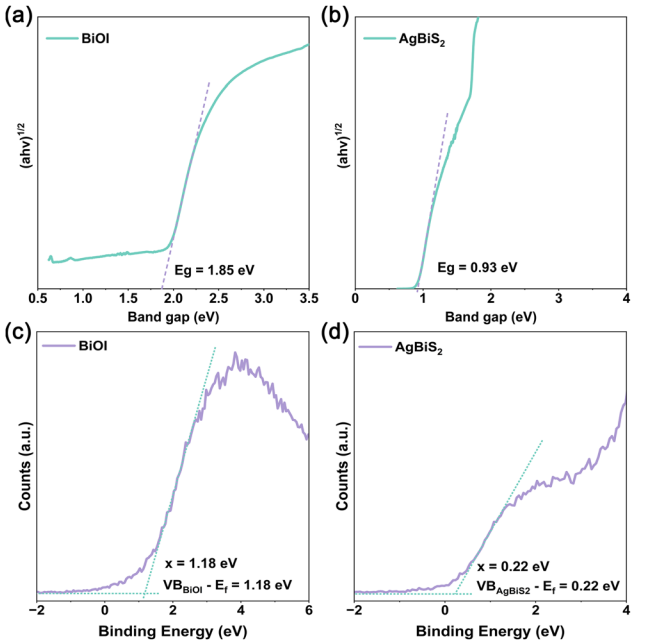

Fig. 4 (a) DRS-Tauc plot curve of BiOI. (b) DRS-Tauc plot curve of $AgBiS_2$. (c) XPS-VB spectrum of BiOI. (d) XPS-VB spectrum of $AgBiS_2$.

removal rate plateaued, reaching only 83% at 25 mg. Consequently, a 7.5 mg dosage of BABS was established as the optimal amount for further degradation studies. Additionally, escalating the TC concentration from 5 mg L^{-1} to 80 mg L^{-1} markedly reduced the removal efficiency from 87% to 27%. Fig. 3(a) demonstrates that under simulated sunlight, the photocatalytic degradation efficiencies of TC by $AgBiS_2$, BiOI, and BABS were 13%, 65%, and 78%, respectively, indicating the superior performance of the BABS heterojunction. However, BABS only degraded 23% of TC under NIR light irradiation for 120 min (Fig. 3(b)). The removal rate of TC was increased to 80% by integrating the BABS heterojunction with $NaYF_4$:Yb,Tm, which fully proved that the upconversion of NIR light by $NaYF_4$:Yb,Tm improved the photocatalytic performance.

To investigate the primary radicals in photocatalysis, *t*-butanol (T-BuOH), disodium edetate (EDTA), and *p*-benzoquinone (BQ) were utilized as scavengers for hydroxyl radicals ($^{\bullet}OH$), holes (h^+), and superoxide radicals ($^{\bullet}O_2^-$), respectively. The results depicted in Fig. S7 (ESI†) show that the presence of T-BuOH led to a mere 10% decrease in TC degradation, suggesting a minor role for $^{\bullet}OH$. Conversely, adding EDTA and BQ reduced the TC degradation rates from 80% to 26% and 21%, respectively, the 54% and 59% decrease highlighted the predominant roles of h^+ and $^{\bullet}O_2^-$ in the photocatalytic process.

The energy band structure of the BABS heterojunction is elucidated through band gap analysis, with BiOI and $AgBiS_2$ exhibiting band gaps of 1.85 eV and 0.93 eV, respectively, as determined by DRS-Tauc curve analysis (Fig. 4(a) and (b)). The Mott–Schottky test revealed BiOI's flat band potential to be 0.08 V *vs.* Ag/AgCl (Fig. S8, ESI†), translating to be 0.28 V *vs.* normal hydrogen electrode (NHE),[25,26] so the Fermi level (E_f) of BiOI is 0.28 eV.[27,28] When the heterojunction is formed, the E_f of BiOI and $AgBiS_2$ will be located at the same energy level,[29] thus the Fermi level (E_f) of $AgBiS_2$ is 0.28 eV. Furthermore, XPS-valence band (VB) spectra indicate the VB to E_f distances for BiOI and $AgBiS_2$ to be 1.18 eV and 0.22 eV, respectively (Fig. 4(c) and (d)). Consequently, the conduction band (CB) and VB positions for BiOI are established at −0.38 eV and 1.46 eV, while for $AgBiS_2$, these positions are −0.43 eV and 0.5 eV, respectively.

Analyzing the band positions of BiOI and $AgBiS_2$ suggests two potential charge transfer pathways. The first involves the formation of a type II heterojunction (Scheme 1(a)), where electrons (e^-) move from CB_{AgBiS2} to CB_{BiOI}, and h^+ transfer oppositely, culminating in the generation of $^{\bullet}O_2^-$ on CB_{BiOI}. Alternatively, a direct Z-type heterojunction may form (Scheme 1(b)), with e^- from CB_{BiOI} recombining with h^+ from VB_{AgBiS2}, leading to the formation of $^{\bullet}O_2^-$ on CB_{AgBiS2}. The CB positions of both these two schemes exceed the redox potential of $O_2/^{\bullet}O_2^-$ (−0.33 V), enabling the production of $^{\bullet}O_2^-$. This is corroborated by the results of the capture experiment. BiOI constitutes 98% of BABS, so it offers more reactive sites. It primarily facilitates the production of $^{\bullet}O_2^-$ in CB_{BiOI}. Therefore, scheme one represents the primary mechanism for photocatalytic enhancement.

We proposed a reasonable photocatalytic enhancement mechanism based on the above characterization results. Specifically, the $NaYF_4$:Yb,Tm component of BABS-Tm converts 980 nm NIR light into multiple wavelengths (365 nm, 450 nm, 475 nm, 647 nm, and 800 nm) and transfers energy to BABS through radiation energy, facilitating indirect photocatalysis (Scheme 1(c)). Concurrently, the $AgBiS_2$ component enhances the system's visible and NIR light absorption, while the BABS heterojunction promotes carrier migration and reduces recombination. Finally, the $^{\bullet}O_2^-$ and h^+ generated in the BABS heterojunction interact with TC to efficiently degrade it into harmless small molecules.

In summary, we successfully synthesized a BABS-Tm ternary heterostructure *via* the hydrothermal method. BABS-Tm enhances the absorption of NIR light in two ways. First, the $AgBiS_2$ component extends the light absorption up to 1500 nm. Second, the $NaYF_4$:Yb,Tm component converts 980 nm NIR light to high-energy visible light, enabling BABS-Tm to degrade

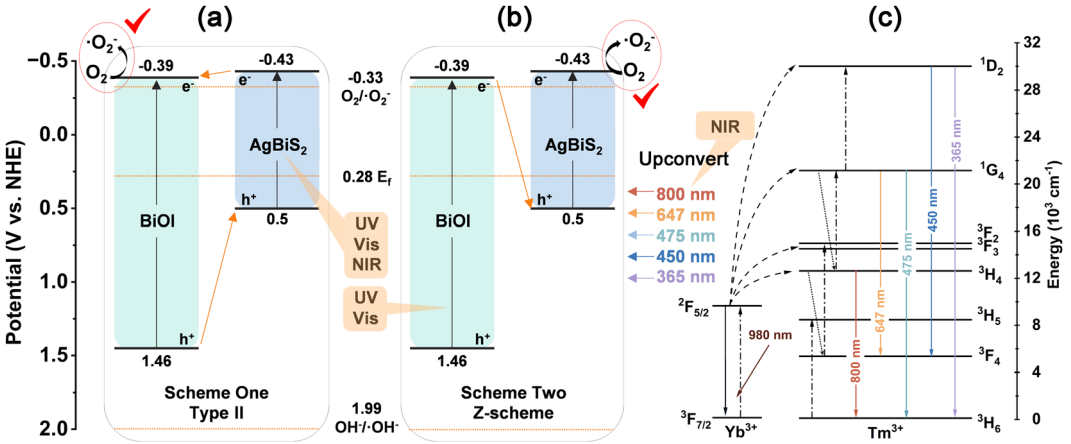

Scheme 1 Schematic illustration of BABS-Tm under UV-vis-NIR irradiation. (a) Type II heterojunction. (b) Z-scheme heterojunction. (c) Schematic energy level diagrams of $NaYF_4$:Yb,Tm under NIR light (980 nm laser) irradiation.

80% of TC under NIR irradiation within 120 min. Additionally, the BABS heterojunction outperforms BiOI and $AgBiS_2$ in terms of photocatalytic activity, attributed to the formation of a heterojunction effectively changing the transfer path of charge carriers and significantly inhibiting the recombination process. This innovative construction extends the photocatalyst's light absorption to the UV-vis-NIR spectrum, optimizing solar energy utilization.

The authors are grateful to the National Natural Science Foundation of China (Grant No. 62074168) and the Natural Science Foundation of Guangdong Province (No. 2024A1 515010729).

Data availability

Data supporting the findings of this study are included in the article and its ESI.† Data are also available upon request.

Conflicts of interest

There are no conflicts to declare.

Notes and references

1 T. Li, N. Tsubaki and Z. Jin, *J. Mater. Sci. Technol.*, 2024, **169**, 82–104.
2 R. Su, Y. Zhu, B. Gao and Q. Li, *Water Res.*, 2024, **251**, 121119.
3 L. Wang, L. Wang, Y. Du, X. Xu and S. X. Dou, *Mater. Today Phys.*, 2021, **16**, 100294.
4 C. Wang, C. Hu, F. Chen, H. Li, Y. Zhang, T. Ma and H. Huang, *Adv. Funct. Mater.*, 2023, **33**, 2301144.
5 J. Nie, X. Zhang, M. Wang, Y. Ou, S. Li, P. Zhong, W. Wang, G. Zhu and X. Ma, *Sep. Purif. Technol.*, 2025, **354**, 128961.
6 C.-Y. Wang, X. Zhang and H.-Q. Yu, *Coord. Chem. Rev.*, 2023, **493**, 215339.
7 L. Guo, H. Huang, L. Mei, M. Li and Y. Zhang, *Mater. Chem. Front.*, 2021, **5**, 2484–2505.
8 Q. Wang, N. Li, M. Tan, M. Deng, G. Yang, Q. Li and H. Du, *Sep. Purif. Technol.*, 2023, **307**, 122733.
9 F. Viñes, M. Bernechea, G. Konstantatos and F. Illas, *Phys. Rev. B*, 2016, **94**, 235203.
10 L. Jiang, Y. Li, J. Peng, L. Cui, R. Li, Y. Xu, W. Li, Y. Li, X. Tian and Q. Lin, *J. Mater. Chem. C*, 2020, **8**, 2436–2441.
11 P. Geng, D. Chen, S. B. Shivarudraiah, X. Chen, L. Guo and J. E. Halpert, *Adv. Sci.*, 2023, **10**, 2300177.
12 M. Abbas, N. Hussain Shah, M. Ilyas, M. Mudasar, A. Raza, M. Ashfaq Ahmad, Y. Cui and Y. Wang, *J. Colloid Interface Sci.*, 2024, **662**, 250–262.
13 Y. Wang, L. Wang, Z. Liu, E. Ye, J. H. Pan, G. Guan and Z. Li, *Appl. Catal., A*, 2022, **644**, 118836.
14 Y. Zhang, X. Zhu and Y. Zhang, *ACS Nano*, 2021, **15**, 3709–3735.
15 Y. Shang, S. Hao, W. Shao, T. Chen, Y. Zhu and C. Yang, *J. Mater. Chem. C*, 2020, **8**, 2847–2851.
16 L. Ma, T. Chen, Q. Li, M. Mai, X. Ye, J. Mai, C. Liu, J. Zhang, D. Lin and X. Ma, *Appl. Surf. Sci.*, 2022, **585**, 152650.
17 H. Wang, X. Tang, Y. Sun, Z. Huang and L. Zhao, *Chem. Eng. J.*, 2024, **480**, 148308.
18 Y. Wu, Z. Cheng, X. Ling, L. Peng and C. Deng, *Mater. Res. Bull.*, 2023, **163**, 112232.
19 X. Linghu, Y. Shu, L. Liu, J. Zhang, Z. Chen, Y. Zhao, Y. Wu, P. Ning, D. Shan and B. Wang, *Environ. Technol. Innovation*, 2022, **28**, 102927.
20 L. Guo, Y. You, H. Huang, N. Tian, T. Ma and Y. Zhang, *J. Colloid Interface Sci.*, 2020, **568**, 139–147.
21 Q. Li, J. Hu, H. Wang and Z. Wu, *Appl. Surf. Sci.*, 2021, **562**, 150250.
22 J. Xing, F. Luo, Y. Qin, X. Chen, Y. Liang, Z. Gao, F. Shang, H. Xu and G. Chen, *J. Mater. Sci. Technol.*, 2023, **138**, 138–148.
23 A. R. Hong, S. Y. Kim, S.-H. Cho, K. Lee and H. S. Jang, *Dyes Pigm.*, 2017, **139**, 831–838.
24 Q. Tian, W. Yao, W. Wu, J. Liu, Z. Wu, L. Liu, Z. Dai and C. Jiang, *ACS Sustainable Chem. Eng.*, 2017, **5**, 10889–10899.
25 S.-H. Chen, X.-Y. Xiao, P.-H. Li, Y.-X. Li, M. Yang, Z. Guo and X.-J. Huang, *Environ. Sci.: Nano*, 2020, **7**, 753–763.
26 C. Chang, H. Yang, W. Mu, Y. Cai, L. Wang, L. Yang and H. Qin, *Appl. Catal., B*, 2019, **254**, 647–658.
27 J.-y Tang, R.-t Guo, W.-g Zhou, C.-y Huang and W.-g Pan, *Appl. Catal., B*, 2018, **237**, 802–810.
28 D. Wu, L. Ye, H. Y. Yip and P. K. Wong, *Catal. Sci. Technol.*, 2017, **7**, 265–271.
29 J. Sun, X. Li, Q. Zhao, M. O. Tadé and S. Liu, *Appl. Catal., B*, 2017, **219**, 259–268.

